Hydrology and
Earth System
Sciences

Open Access

Discussions

EGU

1   Modeling experiments on seasonal lake ice mass and energy

2   balance in Qinghai-Tibet Plateau: A case study

3   Wenfeng Huang[1,2], Bin Cheng[3], Jinrong Zhang[1,2], Zheng Zhang[1,2], Timo Vihma[3],

4   Zhijun Li[4,5], Fujun Niu[5]

5   [1] Key Laboratory of Subsurface Hydrology and Ecological Effects in Arid Region (the Ministry of

6   Education), Chang'an University, Xi'an 710054, China

7   [2] School of Environmental Science and Engineering, Chang'an University, Xi'an 710054, China

8   [3] Finnish Meteorological Institute, Helsinki, Finland

9   [4] State Key Laboratory of Coastal and Offshore Engineering, Dalian University of Technology, Dalian

10   116024, China

11   [5] State Key Laboratory of Frozen Soil Engineering, Northwest Institute of Eco-Environment and

12   Resources, Chinses Academy of Sciences, Lanzhou 730000, China

13   *Correspondence to*: Wenfeng Huang (huangwenfeng@chd.edu.cn)

14

15   **Abstract.** The lake-rich Qinghai-Tibet Plateau (QTP) has significant impacts on regional and global

16   water cycles and monsoon systems through heat and water vapor exchange. The lake-atmosphere

17   interactions have been quantified over open-water periods, yet little is known about the lake ice

18   thermodynamics and heat and mass balance during ice-covered season due to a lack of field data.

19   Modeling experiments on ice evolution and energy balance were performed in a shallow lake with a

20   high-resolution snow and ice thermodynamic model. The bottom ice growth and decay dominated the

21   seasonal evolution of the ~~thickness of~~ lake ice. Strong surface sublimation was a crucial pattern of ice

22   loss, which was up to 40% of the maximum ice thickness. Simulation results matched ~~well with~~ the

23   observations with respect to ice mass balance components, ~~net~~ ice thickness, and ice temperature.

24   Strong solar radiation, consistent freezing air temperature, and low air moisture were the major driving

25   forces controlling the seasonal ice mass balance. Energy balance was estimated at the ice surface and

26   bottom, and within the ice interior and under-ice water. Particularly, almost all heat fluxes showed

27   significant diurnal variations including short- and long-wave radiation, turbulent heat fluxes, water heat

28   fluxes at ice bottom, and absorbed and penetrated solar radiation. The calculated ice surface

29   temperature indicated that the atmospheric boundary layer was consistently stable and neutral over the

30   ice-covered period. The turbulent heat fluxes between the lake ice and air and the net heat gain by the

31   lake were much lower than those during open-water period. ~~Ice surface sublimation (vapor flux) was~~

32   ~~demonstrated to be a vital seasonal water balance component, accounting for 41% of lake water loss~~

33   ~~during the ice seasons.~~

34   ## 1. Introduction

35   The Qinghai-Tibet Plateau (QTP), characterized by a mean altitude of more than 4000 m above sea

36   level (*asl*) and predominated by a freezing climate, is often referred to as the "Third Pole of the Earth".

37   It harbors thousands of lakes covering a total area of approximately 40,700 m and occupying

38   approximately 50% of lakes located in China (Zhang et al., 2014). The QTP is also a headwater region

39   of major Asian rivers including Yangtze, Yellow, Yarlung Tsangpo (Brahmaputra), Mekong, Salween,

40   and Indus Rivers (Immerzeel et al., 2010). Due to its unique climatic environment (e.g. low air pressure

Hydrology and
Earth System
Sciences

Discussions

Open Access

41 and humidity, intense solar radiation, prevailing strong winds, widespread permafrost and glaciers, and
42 dense lake/river network), QTP directly affects the regional and global water cycle, monsoon system,
43 and atmospheric circulations (Wu et al., 2015; Li et al., 2016b; Su et al., 2016).

44   The lakes and ponds in QTP play an crucial role in the surface and subsurface hydrological processes
45 (Pan et al., 2014), moisture and heat budgets (Wang et al., 2015; Li et al., 2016a, c; Wen et al., 2016),
46 regional precipitation (Wen et al., 2015), engineering construction (Niu et al., 2011), and gas emission
47 (Wu et al., 2014). They present dynamic variations on the annual base in terms of numbers and total
48 area. The variations of size are probably due to warming and degradation of permafrost affected by the
49 climate warming through, e.g. thermokarst (Niu et al., 2011), glacier retreating (Liao et al., 2013),
50 increase of precipitation (Lei et al., 2013; Zhang et al., 2014) and strong surface evaporation. Turbulent
51 heat and vapor vapour fluxes at the lake-air interface are crucial driving forces characterizing the
52 lake-air interaction in numerical weather prediction (NWP) and climate models (Yang et al., 2015).

53   Despite the harsh climatic conditions and the difficulties in access to these lakes, some field
54 campaigns have been performed during ice-free periods in recent years using eddy-covariance
55 observations. An unstable or near-neutral atmospheric boundary layer (ABL) prevails over the QTP
56 lake surface in summer (Wang et al., 2015; Li et al., 2015, 2016c). The turbulent heat fluxes show a
57 strong seasonal variation and lag by 2–3 months behind net solar radiation (Li et al., 2016a; Wen et al.,
58 2016). Heat flux dynamics over lake surface differ remarkably from those over other land surface types
59 (like dry/wet grassland) (Biermann et al., 2014), emphasizing the need for a specific parameterization
60 of lakes in surface schemes of NWP and climate models. However, the thermal regimes of lakes in
61 QTP and their impacts on the atmosphere boundary layer and surrounding permafrost during
62 wintertime (ice-covered season) remain unclear. Numerical models and parameterizations can be
63 validated using observational data and will give deep insight into the lake-air interaction and lake
64 thermal regime based on remote sensing datasets of meteorological variables and surface temperature
65 (Kirillin et al., 2017; Wang et al., 2015; Wen et al., 2015).

66   Generally, the QTP lakes and ponds are ice-covered for 3–7 months, depending on their surface area,
67 altitude, and regional climate (Kropáček et al., 2013). Lake ice thermodynamics (ice thickness and
68 temperature) and phenology (the time of freeze-up and break-up, and the duration of the ice cover) play
69 an important role in lake-air interaction (Li et al., 2016a), lake-effect snowfall (Wright et al., 2013),
70 wintertime lake water quality and ecosystems (Kirillin et al., 2012), gas effluxes (Wu et al., 2014), and
71 on-ice transport and operation. All of these issues highlight the accurate representation of QTP lake ice
72 processes. Nevertheless, a few investigations on QTP lake ice have been conducted using field
73 measurements and model simulations. Huang et al. (2012, 2013, 2016) reported the ice processes,
74 interior structure, and thermal property in a small shallow thermokarst lake based on their *in situ*
75 observations of years and provided significant insights into lake ice thermodynamics and its role in
76 local heat and vapor fluxes and lake water budget. High-resolution remote sensing techniques and
77 products were deployed tentatively to retrieve the QTP lake ice processes and provide a promising and
78 convenient tool for lake ice research (Kropáček et al., 2013; Tian et al., 2015).

79   Thermodynamic modeling is an effective and robust methodology to understand lake ice processes
80 and their relationship with local meteorological and hydrological conditions in polar, boreal and
81 temperate regions (Cheng et al., 2014; Semmler et al., 2012; Yang et al., 2012).

82   In this study, we perform a modeling case study of a shallow lake located in the central QTP. Our
83 objectives are (1) to identify major driving force that control the seasonal ice mass balance in QTP
84 thermokarst lakes; (2) to quantify the components of mass and energy balance from the ice surface to

Hydrology and
Earth System
Sciences

Discussions

85   bottom; (3) to estimate the lake-atmosphere heat and vapor fluxes through the whole ice-covered period.

86   To the best of our knowledge, lake ice thermodynamic modeling in QTP has not been carried out before.

87   We expect our work can provide a basis for further in situ measurements and upscaling of lake ice

88   simulations over the QTP.

89   **2. Methodology**

90   **2.1 Site description**

91   The Beiluhe Basin is located in high pluvial and alluvial plain of the central QTP, with an elevation of

92   4500–4600 m *asl* (Fig. 1). The topography is undulating, covered by sparse vegetation and sand dunes.

93   This basin is underlain by continuous permafrost 50-80m thick with the volumetric ice content of 30%–

94   50% (Lin et al., 2017). During years 2004-2014, the mean annual air and ground temperatures varied

95   from -2.9 °C to -4.1 °C and from -1.8 °C to -0.5 °C, respectively (Lin et al., 2017). The annual mean

96   precipitation ranged from 229 to 467 mm (average: 353 mm), while the annual mean potential

97   evaporation ranged from 1588 to 1626 mm (average: 1613 mm) (Lin et al., 2017). There are more than

98   1200 lakes and ponds with the surface area larger than 1000 m^2 in the Beiluhe Basin. The largest lake

99   has a surface area more than 60,000 m^2, and the average is 8500 m^2 (Luo et al., 2015). Lake depths are

100 typically 0.5–2.5 m and the shapes are elliptical or elongated. About 20% of these lakes freeze to the

101 bottom during winter (Lin et al., 2017).

102 Lake BLH-A (unofficial name) is located at 34°49.5′N, 92°55.4′E in Beiluhe Basin. The lake is

103 perennially closed without rivers or streams flowing into and out of it. The minimum and maximum

104 horizontal dimensions of the lake are 120 m and 150 m, respectively, making a total surface area of

105 about 15,000 m^2. The maximum depth is 2.5 m and a stable water level through the year. The water is

106 fresh and has a total dissolved solid of 1.30 g L. Submerged plants grow abundantly in the lake

107 sediment throughout the year. The lake has been investigated using in situ instrumentation and

108 numerical modeling with respect to lake ice physics   (Huang et al., 2011, 2016), hydrothermal regime

109 (Lin et al., 2011), bank retrogression (Niu et al., 2011), and its disturbance to surrounding frozen

110 ground (Lin et al., 2017). Considering physical properties of lake ice, a large number of gas bubbles

111 have been found from the top layer of the ice cover. The large gas content caused a small bulk ice

112 density (880–910 kg m^{-3}) and a small thermal conductivity (1.60–2.10 W m^{-1} K^{-1})) (Huang et al., 2012,

113 2013; Shi et al., 2014).

114 **2.2 Field observations**

115 Field campaigns were conducted in Lake BLH-A through three consecutive winters from 2010/2011 to

116 2012/2013, to record the ice-water-sediment temperatures, air temperature, and surface and bottom

117 growth and decay of the ice cover. All equipments were mounted on a floater moored to the lake bank

118 by four ropes. The floater was placed on the lake surface before the fall freeze-up, thus, all measures

119 were recorded every 30 min through the whole ice season. The data yielded the following information:

120 the dates of freeze-up and break-up (D_f and D_b) and time series of the vertical positions of (a) the

121 ice-water interface (H_b), representing the basal melt or growth, and (b) the air-ice interface (H_s),

122 representing the surface sublimation or/and melting. Hence, the evolution of ice thickness ($H = H_b - H_s$)

123 was detected. For detailed information on instrumentation, see Huang et al. (2016).

124 The Beiluhe weather station (BWS), located 800 m southeast from the lake, monitored the air

125   temperature (T_a), air relative humidity (Rh), atmospheric pressure (P_a), water vapor pressure in the air

126   (e_a), wind speed (V_a) and direction, incident short- and long-wave irradiance (Q_l and Q_s) at 2 m and 10

127   m above the ground surface, and accumulated precipitation (water equivalent, *Prec*). In this paper we

128   focus on the ice season of 2010/2011, when the observed datasets have the highest quality and least

129   missing values. Furthermore, the data reveal a typical seasonal cycle of the lake ice phenology (Fig. 2).

130   In early freezing season in late October, a thin ice layer typically formed at nights and melted during

131   daytime. Finally, a stable ice cover formed in early November (freeze-up). A strong surface sublimation

132   process at the ice-air interface was observed through the whole ice season, reducing the total ice

133   thickness congealed from the ice-water interface. The absolute thickness reached its maximum (~ 60

134   cm) in early February. On the basis of our field visits during freezing (early December) and melting

135   (late March) stages and the constant low temperature and strong wind through the ice season, we

136   concluded that the ice surface was most probably persistently dry throughout the 2010/2011 ice season.

2.3 Thermodynamic snow and ice model

138   A well calibrated (Launiainen and Cheng, 1998, Vihma et al., 2002) and widely used (Cheng et al.,

139   2006, 2008; Semmler et al., 2012; Yang et al., 2012; Cheng et al., 2014) thermodynamic snow and ice

140   model (HIGHTSI) is applied in this study to investigate Lake BLH surface energy and ice mass

141   balances. The surface heat balance reads:

142    $$(1 - \alpha)(1 - \gamma)Q_s + \varepsilon \sigma T_s^4 + Q_{le} + Q_h + Q_p + F_c = F_m \quad (1)$$

143   where Q_s and Q_l is the incident shortwave and longwave radiation, respectively, α is the surface albedo,

144   γ is the fraction of solar radiation penetrating the surface, ε is the thermal emissivity of the surface

145   (ice/snow), σ is the Stefan-Boltzmann constant, T_s is the surface temperature, Q_{le} and Q_h are the latent

146   and sensible heat fluxes, Q_p is the heat flux from precipitation, which can be neglected in QTP during

147   wintertime, F_c is the conductive heat flux in the ice at the surface, and F_m is the surface heat balance.

148   Surface melting is accordingly calculated as:

149    $$\rho_i L_f \frac{dH}{dt} + F_m = k_{iup} \frac{\partial T}{\partial z} \quad (2)$$

150   where ρ_i is the ice density, L_f is the latent heat of freezing, k_{iup} is the thermal conductivity of ice at

151   upper ice layer, T is the ice temperature, and z is the vertical coordinate. The incident short- and

152   longwave radiative fluxes are either parameterized, taking into account cloudiness, or prescribed by

153   observations or NWP model output. The penetration of solar radiation into the snow and ice is

154   parameterized according to surface albedo and optical properties of snow and ice. The turbulent heat

155   fluxes (Q_e and Q_c) at ice-air interface are parameterized using the bulk-aerodynamic formulae as

156   follows:

157    $$Q_{le} = \rho_a L C_e V_a (q_s - q_a) \quad (3)$$

158    $$Q_h = \rho_a c_p C_h V_a (T_s - T_a) \quad (4)$$

159   where ρ_a is the air density, L is the latent heat of sublimation of ice when $T_s < 0°C$ or of evaporation of

160   water when $T_s \geq 0°C$, V_a is the wind speed at the reference height (2.0 m), q_s and T_s are the specific

161   humidity and air temperature at the ice surface, q_a and T_a are the specific humidity and temperature of

162   air at the reference height, and C_e and C_h are the bulk transfer coefficients for heat and water vapor,

163   respectively. Both transfer coefficients are parameterized taking into account the thermal stratification

164   of the atmospheric boundary layer (Launiainen and Cheng, 1998; Wang et al., 2015). In addition, Q_{le}/L

165   gives the equivalent thickness of sublimated ice or of evaporated water E.

166 $$E = \frac{Q_{le}}{L} \qquad (5)$$

167 At the bottom boundary, the ice growth/melt is calculated on the basis of the difference between the

168 heat flux from lake water to ice base (F_w) and the conductive heat flux at the ice bottom layer:

169 $$\rho_i L_f \frac{dH}{dt} + F_w = k_{idn} \frac{\partial T}{\partial z} \qquad (6)$$

170 where k_{idn} is the thermal conductivity of ice at ice bottom layer. In HIGHTSI, F_w is either prescribed as

171 a constant value or prescribed based on in situ observations.

172 The evolutions of thickness and temperature of snow and ice are obtained by solving the heat

173 conduction equations for multiple ice and snow layers. Eq (1) solves the surface temperature, which is

174 used as the upper boundary condition as well as to determine whether surface melting occurs. The ice

175 bottom temperature keeps at the freezing point.

176 **2.4 Meteorological data and model parameters**

177 The meteorological data are based on the BWS (Fig. 3). The 2-m air temperature observed on the lake

178 site was highly correlated with the measurement at BWS station ($R^2 = 0.98$). The T_a has a strong

179 diurnal cycle in response to the large diurnal cycle of solar radiation. The mean T_a was -10.6 °C during

180 simulation period from Day 313 (Nov. 9, 2010) to Day 480 (Apr. 25, 2011). The northwest winds

181 prevailed during the winter season. The gust wind speed was frequently larger than 10 m/s. The average

182 wind speed was 6.5 m s^{-1} associated with an average relative humidity of 34 % only.

183 The daily insolation lasted for 10-12 hours and the average daily solar radiation Qs was about 390 W

184 m^{-2} during the simulation period with the daily maximum ranging from 570 to 1140 W m^{-2}. The

185 averaged downward longwave radiation during daytime (8:00-19:00) and nighttime (20:00-7:00) was

186 approximately 177 and 180 W m^{-2}, respectively. The net longwave cooling was strong during

187 nighttime.

188 The snow pack was very thin, literally zero, during winter 2010/2011. There were a few minor

189 snowfall events, but no snow accumulation because of strong wind. A major detectable snowfall

190 occurred in early April (~ 9 cm of snow), but the snow was blown off in a short time. For simplicity,

191 snow was not taken into account in the model simulation. The transparent ice allowed solar radiation to

192 penetrate into the ice interior and further down to the under-ice water column, heating the ice/water

193 column daily.

194 The sky was persistently clear over the whole ice season 2010/2011. The high cloudiness and

195 overcast condition occurred only during late ice season. A slight thin film of fine sand accumulated on

196 the ice surface in early spring coloring the ice surface light yellow. The surface albedo may have

197 accordingly reduced, leading more solar radiation absorption at and below the surface. An albedo

198 parameterization scheme for a climate system model developed by Briegleb et al., (2004) was applied

199 in this study, but the impact of the surface dust film was not taken into consideration.

200 When running the HIGHTSI model, we have to input values of the heat flux F_w. which is quite

201 challenging to be observed. Actually, we estimate F_w using heat residual method at ice base based on *in*

202 *situ* measurements of in-ice temperature profile and the rate of basal ice growth (Huang et al., to be

203 submitted). But for a reference run, a prescribed time series for the derived F_w was used. The average

204 F_w was approximated 27 W m^{-2}.

205 For the reference run, model forcing data and parameters were given in Table 1.

5

206   **3. Results and analysis**

207   **3.1 Lake ice thickness and mass balance**

208   The BLH-A lake ice congelation lasted from early November to the beginning of February. Through
209   February, the ice growth reached a thermal equilibrium stage, and the ice thickness did not change
210   much. From the beginning of March, the ice started to melt, most at the ice bottom and also within the
211   ice interior. Finally, the ice cover disappeared at the end of April. The growth, thermal equilibrium, and
212   melting periods lasted for approximately 87, 30, and 56 days, respectively.

213   The lake ice mass balance consists of several components (Fig. 4). The ice bottom evolution
214   (congelation ice) dominated the ice growth to 0.75 m until day 430 before a melting started at the ice
215   bottom. The model calculated a total surface melting (~0.12 m) at the end of the ice season. A strong
216   loss of latent heat flux during the entire period generated some 0.23 m of lake ice sublimation at the ice
217   surface. The observed air-ice interface evolution (Fig. 2) revealed the integrated impacts of surface
218   sublimation and melting (during the late season), which could not be instrumentally delineated from
219   each other. By regrouping the modeled ice mass balance components, we can calculate the evolution of
220   the ice surface (i.e. surface sublimation + melting) and ice bottom, and compare them with the
221   measurements (Fig. 4b). Although the modeled bottom depth is 4.2 cm larger than measured one (Table
222   2), the HIGHTSI model very well captured the general evolution both at the ice surface and bottom.
223   The modeled total ice thickness (i.e. $Depth_B–Depth_S$) is in good agreement with the observations (Fig.
224   4c). However, during day 460, the ice melting was stopped due to a snowfall event. This short-term
225   pause was not revealed by the model since the snow thickness was assumed zero.

226   HIGHTSI modeling also affirmed that there are obvious and strong diurnal cycles of freezing and
227   melting at the ice bottom when the ice thickness is less than ~ 20 cm, especially in late spring. For
228   instance, during the melting stage, the ice melts rapidly from 9:00-10:00 to 17:00-18:00, and undergoes
229   an equilibrium or minor growth from 18:00 to 6:00-8:00, then melts again during daytime at the bottom.
230   Besides, the model also detected diurnal variations in the surface sublimation and melting.

231   Statistical analysis indicated that the model results and measurements for ice mass balance have a
232   high correlation (R > 0.97) and small standard deviations (< 3.6 cm), and match very well in terms of
233   surface and bottom depth evolutions and ice thickness with *MAEs* and *RMSEs* generally lower than 5.5
234   cm (Table).

235   **3.2 Lake ice temperatures**

236   The modeled ice temperature regime (Fig. 5) revealed that there are strong diurnal cycles in ice
237   temperature throughout the ice season, following the large diurnal cycle in air temperature and solar
238   radiation. This is consistent with the observed ice thermal dynamics. The calculated surface
239   temperature of ice was continuously lower than the freezing point, except during daytime in late April,
240   when it reveal at the melting point causing some cycles of daytime-melting and nighttime-freezing at
241   the surface.

242   The calculated and observed vertical profiles of ice temperature were compared at selected time
243   steps (Fig. 6). The ice temperature was modeled quite well during the ice growth period (Figs. 6a-d).
244   During the equilibrium and melting stages, the observed and modeled temperature discrepancies were
245   larger especially at the surface and bottom parts. This could have resulted from several processes. From
246   the beginning of the equilibrium stage, the solar radiation increased gradually and was absorbed by the

Hydrology and
Earth System
Sciences
Discussions

Open Access

EGU

247   thermistor sensors at top layer, leading to higher observed values near the surface during daytime (Fig.
248   6e). During the melting period, the bottommost part of the ice column underwent fast phase change,
249   and the inter-crystal spaces could be filled with underlying warm water. The sensors near the ice
250   bottom actually detected the integrated temperature of ice and water, thus the observed temperature
251   could be quite close to and even slightly higher than the freezing point (0 °C) (Figs. 6e,f). On the other
252   hand, the linearly interpolated surface depth is likely to cause errors in determining the true sensor
253   depths within the sublimating ice cover, causing some temperature differences.

254   **3.3 Modeled Energy balance**

255   The lake ice thickening and thinning and temperature regime (i.e. phase transitions) are governed by
256   the energy transport and translation through the air-ice-water column. The good performances of
257   HIGHTSI model in calculating the ice mass balance and temperature dynamics argue comprehensive
258   estimates of heat/radiation transfer and partitioning within the air-ice-water column. For a seasonal
259   cycle, the monthly means of various heat fluxes were calculated at the ice surface, within the ice
260   interior, and at the ice bottom (Table 3).

261   The net shortwave radiation (Q_{sn}) absorbed by the lake acted as a main energy source for ice and
262   water thermodynamics, and followed the seasonal variation of total incident solar radiation (Q_s). The
263   Q_{sn} penetrated through the ice surface and interior, and into the under-ice water column, thus, it was
264   divided into three parts: the net solar radiation used for surface energy balance ($Q_{ss}=(1-\alpha)(1-\gamma)Q_s$)
265   (~43% of Q_{sn}), the absorption by the ice interior beneath surface (Q_{si}) (~36%), and the absorption by
266   water (Q_{sw}) (~21%), all of which also showed similar seasonal variation to Q_s. The water heat flux into
267   ice (F_w) represents the temperature difference between the water and ice bottom, was larger when the
268   ice was thinner. The turbulent heat fluxes did not show strong seasonal variations through the ice
269   season. Furthermore, almost all of the heat fluxes showed strong diurnal variations (Fig. 7). All
270   radiative fluxes (Q_s, Q_{sn}, Q_{si}, and Q_{sw}) had synchronous diurnal cycles, peaked at noon and disappeared
271   through night. The sensible heat flux (Q_h) peaked in the afternoon and had its minimum just before the
272   dawn. The latent heat flux (Q_{le}) had an opposite diurnal pattern with a minimum in the afternoon and
273   maximum in the early morning. The net longwave radiation (Q_{ln}) and surface conductive heat flux (F_c)
274   had a roughly opposite diurnal phase to each other with extremes appeared in the midnight.

275   At the surface (i.e. the surface layer in the model), the upward conductive heat flux (F_c) represents
276   the near surface ice temperature gradient. When the ice was thin (e.g. in November), the larger F_c
277   indicates more heat lost from the ice bottom to surface, and thus rapid ice growth. The net long-wave
278   radiation ($Q_{ln}=Q_l-\varepsilon\sigma T_s^4$) was consistently negative and indicated the cold ice surface emitted the heat
279   back to the air/space all the time. The sensible heat flux (Q_h) was generally positive, thus argued heat
280   gain from the air. The large negative latent heat flux (Q_{le}) (Table 3) manifested the surface sublimation
281   was strong (Fig. 4a). For the surface heat balancing (Eq. 1), the residual F_m was close to zero,
282   indicating a dry cold surface. But in April, its positive value revealed the ice melted at surface (Fig. 4a),
283   and the latent heat was induced by the evaporation of meltwater during late melting season instead of
284   the sublimation of ice.

285   Within the ice interior, the absorbed solar radiation Q_{si} was used to heat the ice during daytime and
286   thus caused the diurnal variation in ice temperature (Fig. 5), and also led to internal melting in way of
287   gas pore expansion during the late ice season (Leppäranta et al., 2010).

288   Beneath the ice bottom, the under-ice water column absorbed the transmitted solar radiation Q_{sw} and
289   raised its temperature at daytime. According to the lake sediment temperature measurements in BLH-A

290 by Lin et al. (2011, 2017), through the whole ice-covered season the bottom sediment releases quite
291 limited heat to lake water (− 0.2~ −0.6 W m^{-2}), consequently, this heat flux can be ignored. For the
292 energy balance of under-ice water, the penetrated solar radiation is the pivotal heat source, of which 56%
293 is released into the ice bottom (F_w), 44% is used to increase the bulk water temperature and partly is
294 transformed to turbulent kinetic energy forcing water convection, and few (< 0.1%) is transported to
295 bottom sediment (permafrost and talik).

3.4 Model experiment on F_w

297 Usual   is assumed to be constant throughout an ice season when simulating ice thickness in Arctic
298 or temperate lakes. Therefore, under the same weather forcing condition, a number of model
299 experiments have been carrying out using constant F_w (0–50 W m^{-2} with an interval of 5 W m^{-2}).

300   During modeling period, the average ice growth at bottom was 0.49 m with a maximum ice growth
301 of about 0.72 m. The average and maximum ice thicknesses were 0.38 m and 0.61 m, respectively.
302 Model experiments indicated that the average F_w cannot be smaller than 15 W m^{-2} because otherwise
303 both average and maximum ice thicknesses differ a lot from observations (Fig. 8). If average F_w is
304 about 35 W m^{-2}, the modeled average and maximum net total ice thickness are not far from the
305 observed values, but have large offsets at ice bottom, especially for the maximum ice growth at ice
306 bottom. If average F_w is more than 35 W m^{-2}, the errors for both average and maximum ice thicknesses
307 are getting larger. It seems when average F_w is between 20 W m^{-2} and 30 W m^{-2}, the modeled results are
308 within the ranges of observed values with respect to total and bottom growth ice thicknesses.

309   In reality, F_w is not a constant value. Model experiments argued that the mass balance at ice base
310 cannot be reproduced using constant F_w through the whole ice season. Based on heat residual method,
311 we created the time series of F_w (Fig. 9) to carry out the reference run (Fig. 4) that gave a very good
312 agreement to the observations.

313   Differ from the ocean and large deep lake, where the variation of F_w is largely driven by the
314 under-ice currents (Krishfield and Perovich, 2005; Rizk et al., 2014), BLH-A was very shallow and the
315 water below ice is largely at a standstill, so the driving force for F_w most likely is the penetrated solar
316 radiation. The modeled solar radiative flux that penetrates through the ice layer and reaches at ice
317 bottom is plotted in Fig. 9. In early simulation, ice was very thin and surface albedo is small, so large
318 part of solar radiation penetrated through ice layer and warmed the underlying water, creating large F_w.
319 When ice was getting thicker, surface albedo increased and penetrated solar radiation was reduced. In
320 later part of the season, melting of ice reduced surface albedo, the downward solar radiation from sky
321 was increased, and thus, more solar radiation was accordingly absorbed in the lake water below ice.
322 The average solar radiation absorbed by under-ice water column during entire simulation period was 22
323 W m^{-2}. Additionally, the specific heat flux from underlying water temperature change was estimated of
324 3 W m^{-2}. The total 25 W m^{-2} is in the range of good agreement between observed and modeled ice
325 thickness (Fig. 8).

4. Discussion

4.1 Implication on ABL over ice-covered lakes

328 The characteristics of the ABL play a direct role in the turbulent heat and mass fluxes and thus the
329 effects of lakes on local and regional monsoon systems and water cycles. Recent findings indicated that

Hydrology and
Earth System
Sciences
Open Access
Discussions
EGU

330 ~~the air-lake energy exchange in QTP is characterized by a persistent unstable air-lake boundary layer~~
331 ~~through the open-water period (Li et al., 2015; Wang et al., 2015; Wen et al., 2016).~~ The modeled and
332 observed temperature profiles of air-ice-water column presented here can give a close insight into the
333 air-lake boundary layer features during the ice-covered period taking the temperature difference
334 between the lake (ice) surface and the air as a bulk stability indicator. The ice surface temperature (T_s)
335 was generally lower than the air temperature (T_a). The monthly mean T_s was consistently lower than the
336 monthly T_a by 1.24 ± 0.55 °C from December through April, indicating a persistent stable atmposphere
337 boundary layer through the ice-covered period (Fig. 10). However, the T_s was 0.31 °C higher than T_a in
338 November when the ice was rapidly growing, especially when the ice thickness was less than ~ 10 cm
339 (i.e., before Nov. 20).
340   Previous investigations revealed that the QTP lakes are predominantly characterized by unstable
341 ABL during open-water period (Li et al., 2015; Wang et al., 2015; Wen et al., 2016). The present results
342 indicated that the air-lake boundary layer turns into a stable or neutral stratification soon after the lake
343 ice forms. When the lake ice disappears, the air boundary layer soon turns into an unstable straitfication
344 again (Wen et al., 2016). However, short-term periods of unstable boundary conditions were observed
345 for approximately 25% of the ice duration period. The unstable conditions usually took up on diurnal
346 scale especially following sudden drops of the air temperature.

347 4.2 The air-lake heat exchange

348 Diurnal changes in turbulent heat fluxes, however, are large which were commonly seen for high
349 latitude and high altitude lakes (e.g. Vesala et al., 2006; Rouse et al., 2008; Nordbo et al., 2011; Wang
350 et al. 2015; Li et al. 2016a, c; Wen et al. 2016). In our study, the mean values of turbulent heat fluxes of
351 Q_h and Q_{le} are 14.1 W m^{-2} and -41.3 W m^{-2}, respectively. These numbers are in line with observations
352 that were obtained in QTP lakes in winter season (Li et al., 2016a). For an intra-annual comparison, the
353 Q_h and Q_{le} over lake ice are approximately 40%–60% lower compared with those over open-water lake,
354 indicating the ice-covered lakes have different heat flux dynamics to the open-water ones. The present
355 turbulent heat fluxes are somehow greater than those observed at Great Slave Lake and a boreal lake in
356 south Finland during open-water period (Blanken et al., 2000; Nordbo et al., 2011). This is attributed to
357 the larger wind speed and drier air prevailing over the QTP.
358   The net heat exchange ($Q_{net} = Q_{sn} + Q_{ln} + Q_h + Q_{le}$) through the atmosphere-lake interface showed strong
359 diurnal and seasonal cycle. Q_{net} increased gradually through the whole ice season. The lake ice released
360 heat into the atmosphere before early March, and then absorbed heat from the atmosphere. Integrated
361 over the ice season, the lake released heat of about 266 MJ m^{-2} (i.e. ~17 W m^{-2}).

362 4.3 Water vapor flux and lake water balance

363 The water balance in a lake reads

364
$$\Delta V = P - E + R_s + R_g \qquad (7)$$

365 where ΔV is the lake water change, and P, E, R_s and R_g are the precipitation, evaporation, net surface
366 inflow and subsurface inflow, respectively.
367   During the freezing season in central QTP, the precipitation is generally quite small and the surface
368 inflow and outflow through gullies and streams are typically blocked due to the freezing conditions.
369 Therefore, the lake water balance is strongly affected by evaporation/sublimation and subsurface
370 inflow/outflow.

Hydrology and
Earth System
Sciences

Open Access

Discussions

371   Assuming ice density of 900 kg m^{-3}, the modeled sublimated ice thickness E can be converted to
372   water equivalent (WE) (Fig. 12). The monthly mean sublimation was the weakest in December and
373   January, but higher in February and March. This is probably due to the higher air temperature, stronger
374   winds, and more incident long- and short-wave radiation than before according to Eqs (3) and (5) (Fig.
375   3). Through the entire ice season, the ice surface water loss due to evaporation/sublimation was
376   approximately 207 mm WE.

377   The BLH-A lake water level observations revealed a decreasing of 0.50 m through the whole ice
378   season (Lin et al., 2017). The surface evaporation/sublimation hence accounts for 41% of lake water
379   loss during the ice-covered period. The remaining part of water loss is probably caused by vertical
380   percolation through the lake sediment to supply deep groundwater, since the talik beneath the lake has
381   developed through the underlying permafrost (Lin et al., 2011, 2017; Niu et al., 2011), and by the
382   lateral water discharge into ambient soil during the thickening and thinning of frozen active layer (Pan
383   et al., 2014; Lin et al., 2017).

384   **5. Summary and conclusion**

385   The ice season was characterized by a freezing period (9 November – 4 February), a thermal
386   equilibrium period (5 February –10 March), and a melting period (11 March – 30 April). During the
387   freezing period, strong atmospheric cooling caused a growth of congelation ice of about 70 cm. The
388   major driving force for ice growth was a consistent subzero air temperature (mean -13 ℃) and a strong
389   average net longwave radiative cooling (-97 W m^{-2}), although the ice surface absorbed a net downward
390   solar radiative flux of 77 W m^{-2} on the average.

391   During melting period, the ice melt rate was about 14 mm/day. Basal melting dominated and surface
392   melting was seen only by the very end of the ice season, because air temperatures remained subzero
393   during most of the winter. A total 0.23 m of ice thickness was lost at the surface due to a sustained
394   sublimation process during the entire study period. This is caused by a combined effect of prevailing
395   strong winds and dry air. The observed average wind speed and relative humidity were 7 m s^{-1} and 34%,
396   respectively.

397   Ice thickness modelled by HIGHTSI was in good agreement with observations, in particular the total
398   ice thickness. The surface sublimation and basal freezing and melting as well as ice temperature
399   regimes were comparable to those observed. The modelled surface energy balance indicated that the net
400   long-wave radiative cooling (-97 W m^{-2}) and upward conductive heat flux in the ice interior as well as
401   turbulent latent heat flux dominated the ice surface energy and mass balance. The average net solar
402   radiative flux was large (181 W m^{-2}); 40% of it was reflected back to the space, 34% was absorbed
403   below the ice surface, and only 26% was used for surface energy balance. Diurnal cycles of surface
404   heat fluxes were driven by the diurnal variations of shortwave radiation. The observed air temperature
405   and calculated ice surface temperature suggested a consistent stably stratified ABL uring most of the
406   ice-covered period, except when the ice thickness was less than ~10 cm. Through the whole
407   ice-covered season, the lake (ice) released 17 W m^{-2} heat to the atmosphere.

408   The ice surface mass balance was dominated by surface ice sublimation, which was modeled very
409   well. The sublimation was demonstrated to be a key component for lake water balance and accounted
410   for 41% of lake water loss during wintertime. In light of the generally low air humidity and strong wind
411   over QTP, the sublimation can be critical for the water balance of a large number of shallow lakes and
412   ponds over the QTP, and further research (obs and mod) is needed for the quantification of sublimation

413   in a regional scale over QTP.

414   The water-ice heat flux F_w controlled the basal, and thus, the net ice thickness evolution. The model
415   experiments indicated that constant F_w through the whole ice season cannot produce a reasonable basal
416   mass balance. A parameterized time series of F_w was used and gave realistic results. This confirmed the
417   temporal variation in F_w in shallow QTP thermokarst lakes. Many more observing efforts should be
418   made to quantify it and its governing physics.

419   The present modeling indicated that the largest uncertainty for QTP lake ice modeling is the effect of
420   F_w. Thermokarst lakes on QTP are typically shallow and small, without significant surface water input
421   and output, implying that through-lake current or lake-wide circulation under the ice cover are
422   negligible (Kirillin et al., 2015). Cold sediment layer limits heat release into the overlying water (Lin et
423   al., 2011). However, the solar radiation is strong (due to persistent clear sky condition), and the lake ice
424   cover is consistently free of snow. In QTP, the surface albedo of ice in large lakes can be
425   unprecedentedly small (Li et al., 2018). Indeed, in our study the Briegleb albedo scheme yielded small
426   albedo, in particular, when the ice was thin. Intensive penetrative solar radiation can drive under-ice
427   turbulent mass and heat mixing (Mironov et al., 2002), however, the quantitative effect of solar
428   penetration on F_w is still not yet know, and needs new field experiments.

429   Snow is neglected in this modeling work, however, snowfall occasionally occur on QTP and it may
430   have a strong impact in ice mass balance, especially for large lakes (Cheng et al., 2014). The major
431   impact of snow on ice thermodynamics is the insulation effect (Leppäranta, 2015). Snow-ice is not
432   likely to form on QTP, since in early winter the air temperature drops fast and the ice freezes quickly.
433   However, superimposed ice may happen in late spring if there is thick snow on top of ice. Otherwise,
434   snow can compensate the strong ice mass loss due to sublimation, cutting down water loss in QTP
435   lakes in winters.

436

References

448   Biermann, T., Babel, W., Ma, W., Chen, X., Thiem, E., Ma. Y., and Foken, T.: Turbulent flux
449   observations and modeling over a shallow lake and a wet grassland in the Nam Co basin,
450   Tibetan Plateau, Theor. Appl. Climatol., 116, 301-316, 2014.
451   Blanken, P.D., Rouse, W.R., Culf, A.D., Spence, C., Boudreau, L.D., Jasper, J.N., Kochtubajda, B.,
452   Schertzer, W.M., Marsh, P., and Verseghy, D.: Eddy covariance measurements of evaporation

Hydrology and
Earth System
Sciences
Discussions

Open Access

EGU

453   from Great Slave Lake, Northwest Territories, Canada, Water Res. Res., 36(4), 1069-1077,
454   2000.
455   Briegleb, B., Bitz, C.M., Hunke, E.C., Lipscomb, W.H., Holland, M.M., Schramm, J., and Moritz,
456   R.: Scientific description of the sea ice component in the Community Climate System Model,
457   Ver. 3, NCAR/TN-463+STR, NCAR Tech Note, 1-78, 2004.
458   Cheng, B., Vihma, T., Rontu, L., Kontu, A.: Evolution of snow and ice temperature, thickness and
459   energy balance in Lake Orajärvi, northern Finland, Tellus A, 66, 21564,
460   http://dx.doi.org/10.3402/tellusa.v66.21564, 2014.
461   Cheng, B., Vihma, T., Pirazzini, R., and Granskog, M.: Modeling of superimposed ice formation
462   during spring snowmelt period in the Baltic Sea, Ann. Glaciol., 44, 139–146, 2006.
463   Cheng, B., Zhang, Z., Vihma, T., Johansson, M., Bian, L., Li, Z., and Wu, H.: Model experiments
464   on snow and ice thermodynamics in the Arctic Ocean with CHINARE 2003 data, J. Geophys.
465   Res., 113, C09020, doi:10.1029/2007JC004654, 2008.
466   Huang, W., Han, H., Shi, L., Niu, F., Deng, Y., and Li, Z.: Effective thermal conductivity of
467   thermokarst lake in Beiluhe Basin, Qinghai-Tibet Plateau, Cold Reg. Sci. Technol., 85, 34-41,
468   2013.
469   Huang, W., Li, R., Han, H., Niu, F., Wu, Q., and Wang, W.: Ice processes and surface ablation in a
470   shallow thermokarst lake in the central Qinghai-Tibet Plateau, Ann. Glaciol., 57(71), 20-28,
471   2016.
472   Huang, W., Li, Z., Han, H., Niu, F., Lin, Z., and Leppäranta, M.: Structural analysis of thermokarst
473   lake ice in Beiluhe Basin, Qinghai-Tibet Plateau, Cold Reg. Sci. Technol., 72, 33-42, 2012.
474   Immerzeel, W.W., van Beek, L.P.H., and Bierkens, M.F.P.: Climate change will affect the Asian
475   water towers, Science, 328, 1382-1385, 2010.
476   Jonas, T., Terzhevik, A.Y., Mironov, D.V., and Wüest, A.: Radiatively driven convection in an
477   ice-covered lake investigated by using temperature microstructure technique, J. Geophys. Res.,
478   108(C6), 3183, doi: 10.1029/2002JC001316, 2003.
479   Kirillin, G.B., Forrest, A.L. Graves, K.E., Fischer, A., Engelhardt, C., and Laval, B.E.:
480   Axisymmetric circulation driven by marginal heating in ice-covered lakes, Geophys. Res. Lett.,
481   42, 2893-2900, 2015.
482   Kirillin, G., Leppäranta, M., Terzhevik, A., Granin, N., Bernhardt, J., Engelhardt, C., Efremova, T.,
483   Golosov, S., Palshin, N., Sherstyankin, P., Zdorovennova, G., and Zdorovennov, R.: Physics of
484   seasonally ice-covered lakes: a review, Aquat. Sci., 74(4), 659-682, 2012.
485   Kirillin, G., Wen, L., and Shatwell, T.: Seasonal thermal regime and climatic trends in lakes of the
486   Tibetan Highlands, Hydrol. Earth Syst. Sci., 21, 1895-1909, 2017.
487   Krishfield, R.A., and Perovich, D.K.: Spatial and temporal variability of oceanic heat flux to the
488   Arctic ice pack, J. Geophys. Res., 110, C07021, doi: 10.1029/2004JC002293, 2005.
489   Kropáček, J., Maussion, F., Chen, F., Hoerz, S., and Hochschild, V.: Analysis of ice phenology of
490   lakes on the Tibetan Plateau from MODIS data, The Cryosphere, 7, 287-301, 2013.
491   Launiainen, J., and Cheng, B.: Modeling of ice thermodynamics in natural water bodies, Cold Reg.
492   Sci. Technol., 27(3), 13-178, 1998.
493   Lei, Y., Yao, T., Bird, B. W., Yang, K., Zhai, J., and Sheng, Y.: Coherent lake growth on the central
494   Tibetan Plateau since the 1970s: Characterization and attribution, J. Hydrol., 483(3), 61-67,
495   2013.
496   Leppäranta, M.: Freezing of lakes and the evolution of their ice cover, Springer, Berlin,

497   Heidelberg, 2015.

498   Leppäranta, M., Terzhevik, A., and Shirasawa, K.: Solar radiation and ice melting in Lake
499   Vendyurskoe, Russian, Hydrol. Res., 41(1), 50-62, 2010.

500   Li, X., Ma, Y., Huang, Y., Hu, X., Wu, X., Wang, P., Li, G., Zhang, S., Wu, H., Jiang, Z., Cui, B.,
501   and Liu, L.: Evaporation and surface energy budget over the largest high-altitude saline lake
502   on the Qinghai-Tibet Plateau, J. Geophys. Res.- Atmos., 121(18), 10470-10485, 2016a.

503   Li, Y., Zhang, C., and Wang, Y.: The verification of millennial-scale monsoon water vapor
504   transport channel in northwest China, J. Hydrol., 536, 273-283, 2016b.

505   Li, Z., Ao, Y., Lyu, S., Lang, J., Wen, L., Stepanenko, V., Meng, X., and Zhao, L.: Investigations of
506   the ice surface albedo in the Tibetan Plateau lakes based on the field observation and MODIS
507   products, J. Glaciol., doi: 10.1017/jog.2018.35, 2018.

508   Li, Z., Lyu, S., Zhao, L., Wen, L., Ao, Y., and Wang, S.: Turbulent transfer coefficient and
509   roughness length in a high-altitude lake, Tibetan Plateau, Theor. Appl. Climatol., 124, 723-735,
510   2016c.

511   Li, Z., Lyu, S., Ao, Y., Wen, L., Zhao, L., and Wang, S.: Long-term energy flux and radiation
512   balance observations over Lake Ngoring, Tibetan Plateau, Atmos. Res., 155, 13-25, 2015.

513   Liao, J., Shen, G., and Li, Y.: Lake variations in response to climate change in the Tibetan Plateau
514   in the past 40 years, Int. J. Digit. Earth, 6(6), 534-549, doi:10.1080/17538947.2012.656290,
515   2013.

516   Lin, Z.J., Niu, F.J., Fang, J.H., Luo, J., and Yin, G.A.: Interannual variations in the hydrothermal
517   regime around a thermokarst lake in Beiluhe, Qinghai-Tibet Plateau, Geomorphology, 276,
518   16-26, 2017.

519   Lin, Z., Niu, F., Liu, H., and Lu, J.: Hydrothermal processes of alpine tundra lakes, Beiluhe Basin,
520   Qinghai-Tibet Plateau, Cold Reg. Sci. Technol., 65, 446-455, 2011.

521   Luo, J., Niu, F., Lin, Z., Liu, M., and Yin, M.: Thermokarst lake changes between 1969 and 2010
522   in the Beilu River Basin, Qinghai-Tibet Plateau, Chinese Sci. Bull., 60(5), 556-564, 2015.

523   Mironov, D., Terzhevik, A., Kirillin, G., Jonas, T., Malm, J. and Farmer, D.: Radiatively driven
524   convection in ice-covered lakes: Observations, scaling, and a mixed layer model, J. Geophys.
525   Res., 107(C4), 3032, doi: 10.1029/2001JC000982, 2002.

526   Mountain Research Initiative EDW Working Group: Elevation-dependent warming in mountain
527   regions of the world, Nature Clim. Change, 5, 424-430, 2015.

528   Niu, F., Lin, Z., Liu, H., and Lu, J.: Characteristics of thermokarst lakes and their influence on
529   permafrost in Qinghai-Tibet Plateau, Geomorphology, 132, 222-233, 2011.

530   Nordbo, A., Launiainen, S., Mammarella, I., Leppäranta, M., Houtari, J., Ojala, A., and Vesala, T.:
531   Long-term energy flux measurements and energy balance over a small boreal lake using eddy
532   covariance technique, J. Geophys. Res., 116, D02119, doi: 10.1029/2010JD014542, 2011.

533   Pan, X., Yu, Q., and You, Y.: Role of rainwater induced subsurface flow in water-level dynamics
534   and thermoerosion of shallow thermokarst ponds on the Northeastern Qinghai-Tibet Plateau,
535   The Cryosphere Discuss., 8, 6117-6146, 2014.

536   Rizk, W., Kirillin, G., and Leppäranta, M.: Basin-scale circulation and heat fluxes in ice-covered
537   lakes, Limnol. Oceanogr., 59(2), 445-464, , 2014.

538   Semmler, T., Cheng, B., Yang, Y., and Rontu, L.: Snow and ice on Bear Lake (Alaska)-sensitivity
539   experiments with two lake ice models, Tellus A, 64, 17339, doi:10.3402/tellusa.v64i0.17339,
540   2012.

541 Shi, L., Li, Z., Niu, F., Huang, W., Lu, P., Feng, E., and Han, H.: Thermal diffusivity of
542 thermokarst lake ice in the Beiluhe basin of the Qinghai-Tibet Plateau, Ann. Glaciol., 55(66),
543 153-158, 2014.
544 Su, F., Zhang, L., Ou, T., Chen, D., Yao, T., Tong, K., and Qi, Y.: Hydrological response to future
545 climate changes for the major upstream river basins in the Tibetan Plateau, Global Planet.
546 Change, 136, 82-95, 2016.
547 Tian, B., Li, Z., Engram, M. J., Niu, F., Tang, P., Zou, P., and Xu, J.: Characterizing C-band
548 backscattering from thermokarst lake ice on the Qinghai-Tibet Plateau, ISPRS J. Photogramm.
549 Remote Sens., 104, 63-76, 2015.
550 Vesala, T., Houtari, J., Rannik, U., Suni, T., Smolander, S., Sogachev, A., Launiainen, S., and Ojala,
551 A.: Eddy covariance measurements of carbon exchange and latent and sensible heat fluxes
552 over a boreal lake for a full open-water period, J. Geophys. Res., 111, D11101, doi:
553 10.1029/2005JD006365, 2006.
554 Wang, B., Ma, Y., Chen, X., Ma, W., Su, Z., and Menenti, M.: Observation and simulation of
555 lake-air heat and water transfer processes in a high-altitude shallow lake on the Tibetan Plateau,
556 J. Geophys. Res., 120, 12327-12344, 2015.
557 Wen, L., Lyu, S., Kirillin, G., Li, Z., and Zhao, L.: Air-lake boundary layer and performance of a
558 simple lake parameterization scheme over the Tibetan highlands, Tellus A, 68, 31091,
559 doi:10.3402/tellusa.v68.31091, 2016.
560 Wen, L., Lyu, S., Li, Z., Zhao, L., and Nagabhatla, N.: Impacts of the two biggest lakes on local
561 temperature and precipitation in the Yellow River Source Region of the Tibetan Plateau, Adv.
562 Meteorol., 2015, 248031, doi:10.1155/2015/248031, 2015.
563 Wright, D.M., Posselt, D.J., and Steiner, A.L.: Sensitivity of lake-effect snowfall to lake ice cover
564 and temperature in the Great Lakes region, Mon. Weather Rev., 141, 670-689, 2013.
565 Wu, G., Duan, A., Liu, Y., Mao, J., Ren, R., Bao, Q., He, B., Liu, B., and Hu, W.: Tibetan Plateau
566 climate dynamics: recent research progress and outlook, Natl. Sci. Rev., 2, 100-116, , 2015.
567 Wu, Q., Zhang, P., Jiang, G., Yang, Y., Deng, Y., and Wang, X.: Bubble emissions from
568 thermokarst lakes in the Qinghai-Xizang Plateau, Quatern. Int., 321, 65-70, 2014.
569 Yang, K., Ye, B., Zhou, D., Foken, T., Qin, J., and Zhou, Z.: Response of hydrological cycle to
570 recent climate changes in Tibetan Plateau, Climatic Change, 109, 517-534, 2011.
571 Yang, X., Lyu, Y., Ma, Y., and Wen, J.: Summertime thermally-induced circulations over the Lake
572 Nam Co region of the Tibetan Plateau, J. Meteorol. Res., 29(2), 305-314, 2015.
573 Yang, Y., Leppäranta, M., Cheng, B., Heil, P., Li, Z.: Numerical modeling of snow and ice
574 thickness in Lake Vanajärvesi, Finland, Tellus A, 64, 17202, doi:10.3402/tellusa.v64i0.17202,
575 2012.
576 Zhang. G., Yao, T., Xie, H., Zhang, K., and Zhu, F.: Lakes' state and abundance across the Tibetan
577 Plateau, Chinese Sci. Bull., 59(24), 3010-3021, 2014.

Table 1. Parameters and input data applied in the model reference run

Variables	Value	Source
V_a, T_a, Rh, Q_s, Q_l	Time series	Observations at BWS
Ice density ρ_i	900 kg m^{-3}	Huang et al. (2012, 2013)
Thermal conductivity k_i	1.80 W m^{-1} K^{-1}	Huang et al. (2013)
Albedo α	0.1- 0.55	Briegleb et al. (2004)
Ice extinction coefficient κ_i	(1.5–17) m^{-1}	Launiainen and Cheng (1998) adapted from Grenfell and Maykut (1977)
Bottom heat flux F_w	Time series	Parameterized based on in-ice temperature profile and ice bottom growth rate (Huang et al., to be submitted)
Initial ice thickness	0.05 m	Observation
Initial ice temperature	Linear interpolation between T_a and T_b	Calculation

Table 2. The mean bias error (*MBE*), mean absolute error (*MAE*), standard deviation (*STD*), root mean square error (*RMSE*), and correlation coefficient (*R*) between modeled and observed ice mass balance components with *n*=4023 (in cm)

Items	Surface	Bottom	Total mass balance
MBE	0.2	4.2	4.1
MAE	2.5	4.8	4.3
STD	2.9	3.6	3.0
RMSE	2.9	5.5	5.0
R	0.97	0.99	0.99

Table 3. The monthly means of heat fluxes (in W m^{-2}) within the air-ice-water column. Q_s: incident solar radiation; Q_{sn}: net solar radiation; Q_{ss}: net solar radiation for surface heat balance; Q_{ln}: net longwave radiation; Q_h: sensible heat flux; Q_{le}: latent heat flux; F_c: surface conductive heat flux; F_m: net surface heat flux, that is, the sum of Q_{ss}, Q_{ln}, Q_h, Q_{le} and F_c; Q_{si}: solar radiation absorption within the ice interior; Q_{sw}: solar radiation into under-ice water; F_w: heat flux from water into ice.

Month	11	12	1	2	3	4
Q_s	162	142	138	176	208	259
Q_{sn}	110	69	63	110	135	169
Q_{ss}	37	30	32	57	65	62
Q_{ln}	-112	-100	-83	-87	-79	-73
Q_h	-10	15	15	17	-1	4
Q_{le}	-46	-31	-32	-54	-53	-53
F_c	125	85	68	68	69	63
F_m	-6	-0.1	0.1	0.2	2	4
Q_{si}	35	26	23	40	49	63
Q_{sw}	39	14	8	14	21	43
F_w	34	21	20	20	21	36
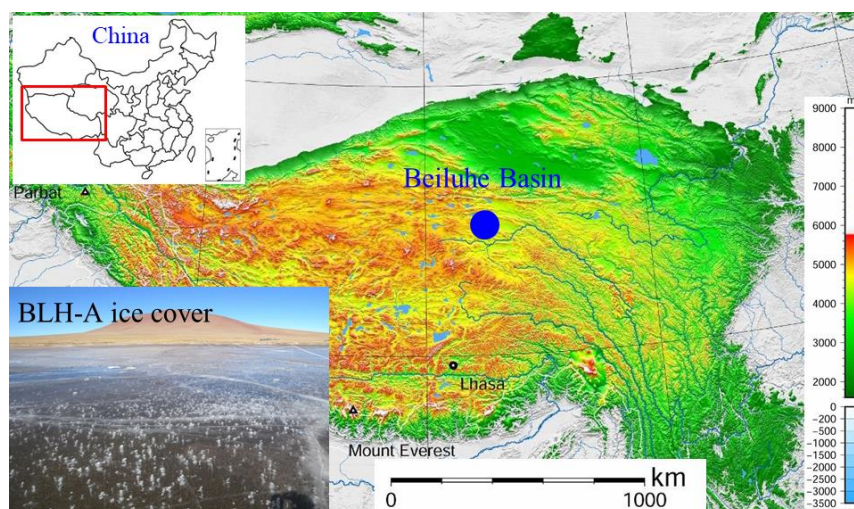
Figure 1. General view of QTP and location of the study area
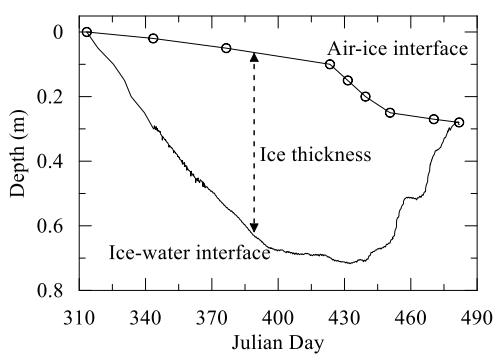
Figure 2. The observed lake ice thickness evolution over the whole 2010/2011 ice season. The open circles denote the observed location of the ice surface, and the solid lines connecting the circles denote the linear interpolation.
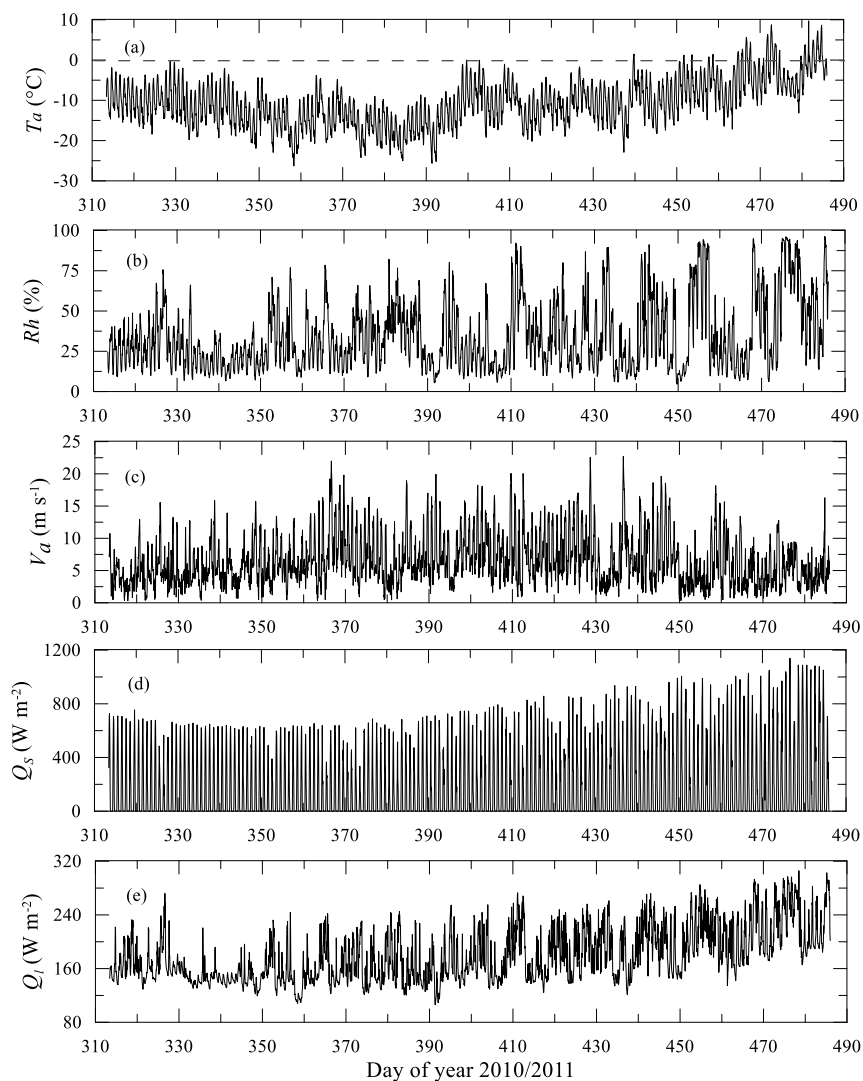
Figure 3. The time series of observed meteorological variables through the whole ice season of 2010-2011. (a) daily mean air temperature T_a, (b) relative humidity Rh, (c) wind speed V_a, (d) incident shortwave solar radiation Q_s, and (e) incident longwave radiation Q_l.
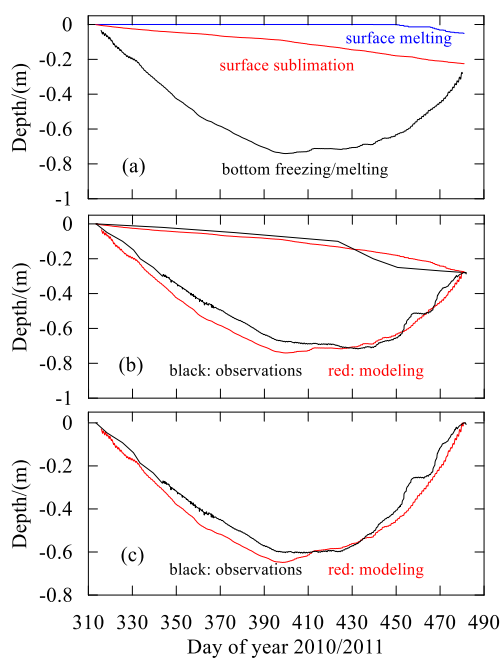
Figure 4. The HIGHTSI modeled BLH lake ice mass balance components (a), the ice surface and bottom evolution (b), and the ice thickness (c).
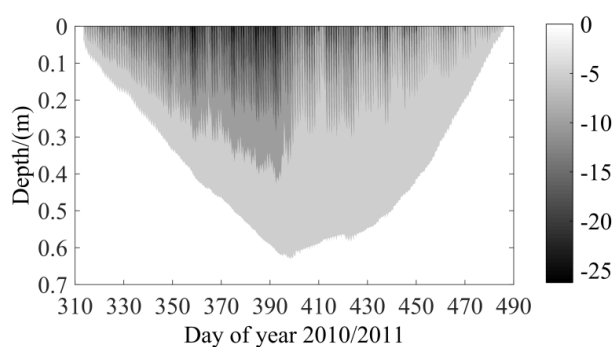
Figure 5. HIGHTSI modeled ice temperature regime for winter 2010/2011.
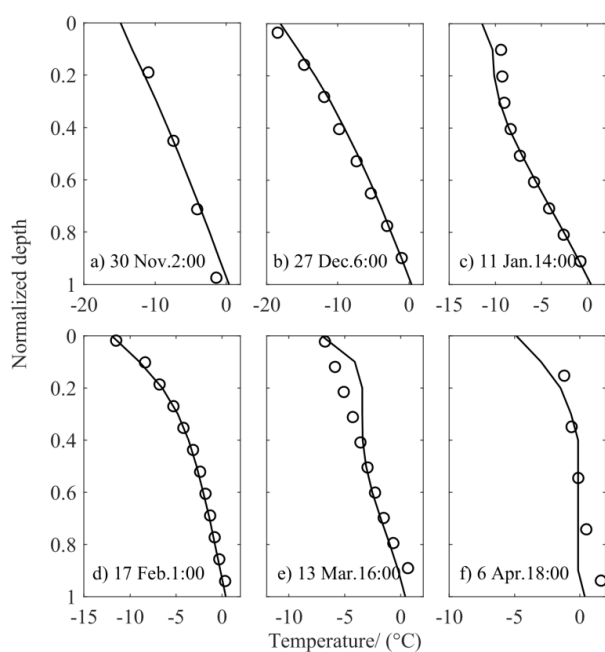
Figure 6. Comparisons of modeled (lines) and observed (circles) vertical temperature profiles of within ice at selected time steps. A normalized depth (depth divided by ice thickness) is used as the y-axis (0 and 1 denote the ice surface and bottom, respectively).
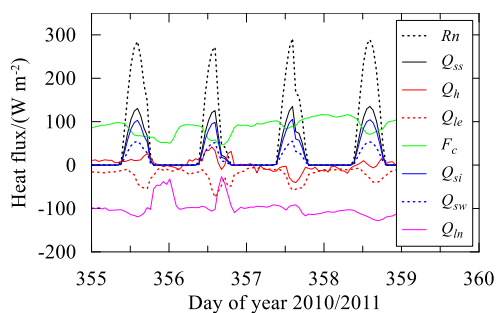
Figure 7. Diurnal patterns of various radiation/heat flux
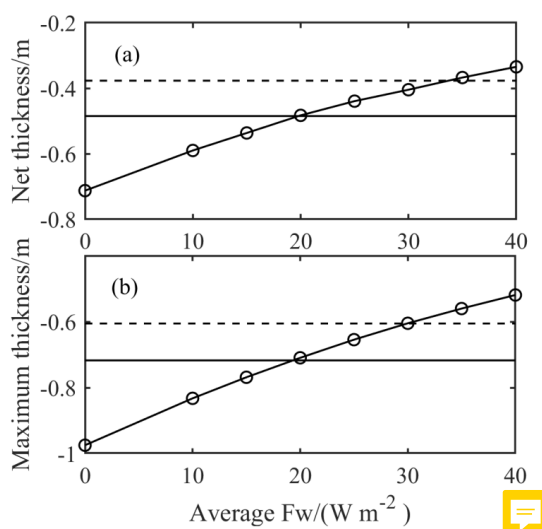
Figure 8. Modeled (lines with circles) average (a) and maximum (b) ice thickness applying different constant F_w. The broken lines are observed average and maximum ice thickness during the simulation period. The solid lines are observed average and maximum ice growth at ice bottom.
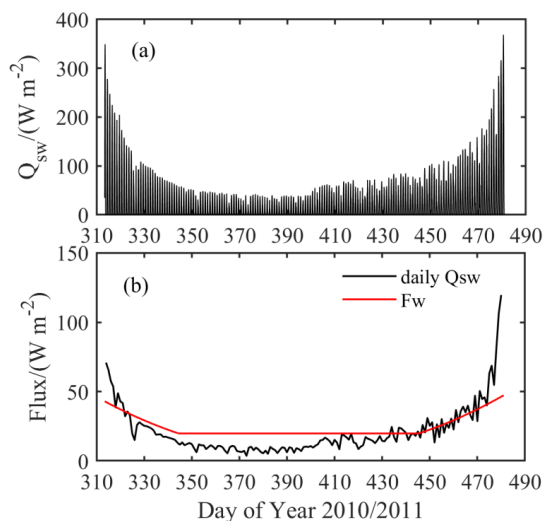
Figure 9. Modeled solar radiation penetration (Q_{sw}) into the under-ice water column: hourly (a) and daily averages (b) with prescribed F_w during the simulation period.
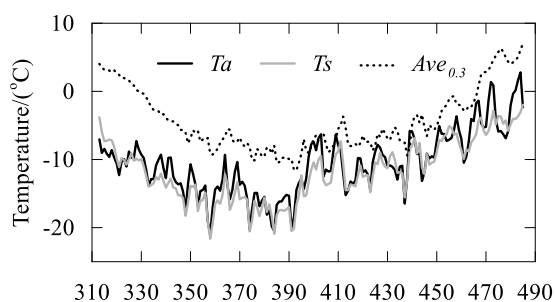

Figure 10. Daily means of the observed air temperature (T_a), the averaged ice/water temperature of the top 30 cm ($Ave_{0-0.3}$), and the calculated ice surface temperature (T_s).
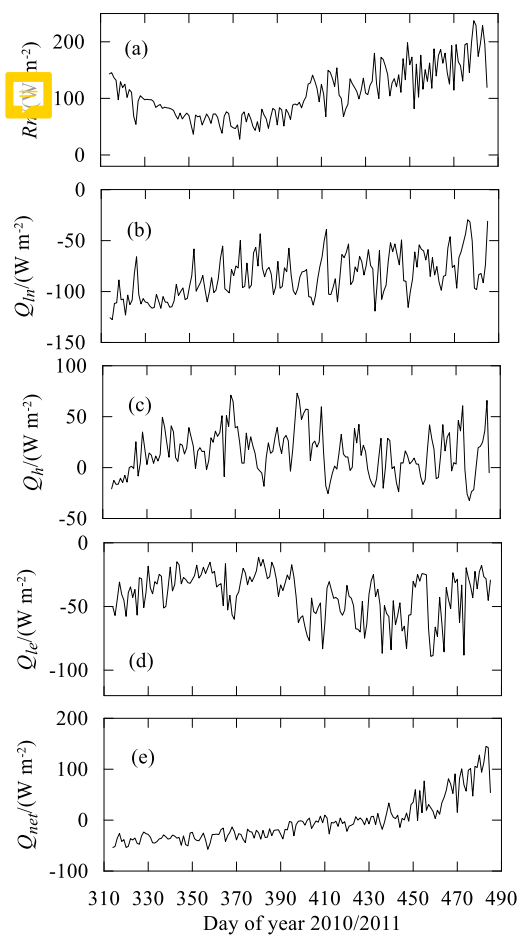
Figure 11. Daily means of the surface energy balance components of net shortwave (Q_{sn}) and longwave (Q_{ln}) radiation, turbulent sensible (Q_h) and latent (Q_e) heat fluxes, and net flux into the lake ($Q_{net}= Q_{sn}+Q_{ln}+Q_h+Q_{le}$) though the entire ice season.

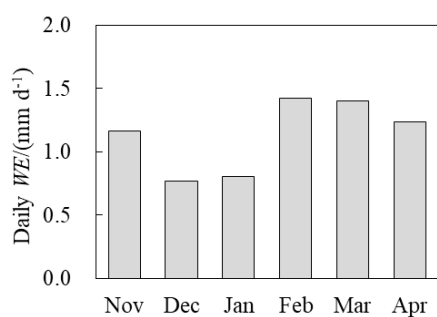**Figure 12.** The daily mean surface sublimated water equivalent through the winter 2010/2011.